Submitted to the 29th International Conference on High-Energy Physics ICHEP98, Vancouver, Canada, July 1998

Measurement of Internal Jet Structure in Dijet Production in Deep-Inelastic Scattering

H1 Collaboration

Abstract

Internal jet structure in dijet production in deep-inelastic scattering is measured with the H1 detector at HERA. In the kinematical region of squared momentum transfers of $10 < Q^2 \lesssim 120\,\mathrm{GeV}^2$ and x-Bjorken values of $2 \cdot 10^{-4} \lesssim x_{Bj} \lesssim 8 \cdot 10^{-3}$ jets with transverse energies of $E_{\perp\mathrm{Breit}} > 5\,\mathrm{GeV}$ are selected in the Breit frame employing $k_\perp$ and cone jet algorithms. Measured observables are jet shapes and subjet multiplicities as a function of a resolution parameter. Both observables are corrected for detector effects and presented as functions of the transverse jet energy and jet pseudo-rapidity. The corrected data are well described by QCD models. A dependence of the jet broadness and the average number of subjets on the transverse energy and the pseudo-rapidity of the jet is observed. With increasing transverse jet energies and decreasing pseudo-rapidities, i.e. towards the photon hemisphere, the jets are more collimated. Furthermore the jets defined by the $k_\perp$ algorithm turn out to be narrower than jets defined by the cone algorithm.

Abstract: 532
Parallel sessions: 3,5
Plenary sessions: 5,7

1 Introduction

A sizable fraction of the final states produced in high energy collisions shows the characteristic feature of large amounts of hadronic energy in small angular regions. These collimated sprays of hadrons are called jets. They are the observable signals of the underlying short distance processes and are the subject of many quantitative studies and used to test the predictions of perturbative QCD. An important prerequisite for the study of jet production rates is the understanding of their detailed properties.

The internal structure of jets is sensitive to the mechanism of how a complex aggregate of observable hadrons evolves from a hard process. The understanding of this mechanism involves higher orders of the strong coupling constant in perturbation theory as well as large non-perturbative contributions. This is a challenging task for theory. Recently some approaches lead to encouraging results [1, 2].

The internal structure of jets has been studied in e^+e^- [3] and in hadron-hadron collisions [4]. At the $e^{\pm}p$ collider HERA, jets can be studied over a wide range of transverse jet energies $E_\perp$ and in different pseudorapidity regions. These investigation can be performed in photoproduction ($Q^2 \approx 0\ \mathrm{GeV}^2$) as well as in deep-inelastic scattering (DIS) at large squared four momentum transfers Q^2. In a previous publication we have measured the $E_\perp$ dependence of the jet width [5] in photoproduction. Recently jet shapes have been investigated in photoproduction [6] and in DIS at $Q^2 > 100\ \mathrm{GeV}^2$ [7].

In this paper we present measurements of internal jet structure in the Breit frame where the transverse jet energies[1] ($E_{\perp\text{Breit}}$) directly reflect the hardness of the underlying QCD process. The analysis has been performed on an inclusive dijet sample at $10 < Q^2 \lesssim 120\,\mathrm{GeV}^2$ and $E_{\perp\text{Breit}} > 5$ GeV. The analysis is based on data taken in 1994 with the H1 detector at HERA where 27.5 GeV positrons collided with 820 GeV protons. The data correspond to an integrated luminosity of $\mathcal{L}_{int} \simeq 2\,\mathrm{pb}^{-1}$.

Jets are defined in the Breit frame by $k_\perp$ and cone jet algorithms. Two observables, jet shapes and subjet multiplicities, are studied. The jet shape, defined as the average fractional transverse energy of a jet inside a subcone around the jet axis, is a natural choice for the study of internal jet structure for cone jet definitions.

For the $k_\perp$ cluster algorithm we have also measured the multiplicity of subjets, resolved at a resolution scale which is a fraction of the jet's transverse energy. Both observables are presented as functions of the transverse jet energy and the pseudo-rapidity[2] of the jets in the Breit frame. We confront the predictions of QCD models with our data.

The paper is organized as follows: In section 2 we introduce the jet algorithms used in the analysis and give the exact definition of the measured observables in section 3. In section 4 we describe the QCD models used for the correction of the data and to which the results are compared. Section 5 gives a brief description of the H1 detector. The data selection and the correction procedure are described in sections 6 and 7 and the results are discussed in section 8.

[1] "transverse" refers to the z-axis which is given by the axis of the virtual photon and the proton.

[2] The pseudo-rapidity η is defined as $\eta \equiv -\ln(\tan\theta/2)$ where θ is the polar angle with respect to the proton direction. This definition is chosen in both the laboratory frame and the Breit frame.

2 Jet Definitions

In the following analysis we are using two different jet definitions: A cone algorithm and a $k_\perp$ cluster algorithm, which are both applied to the particles boosted into the Breit frame. The recombination of particles is done in the $E_\perp$ recombination scheme which is based on quantities, transverse energy $E_\perp$, pseudo-rapidity η and azimuthal angle ϕ. The axis of a jet is defined by

$$E_{\perp,jet} = \sum_{i \in jet} E_{\perp,i}, \qquad \eta_{jet} = \frac{\sum_i E_{\perp,i}\ \eta_i}{\sum_i E_{\perp,i}}, \qquad \phi_{jet} = \frac{\sum_i E_{\perp,i}\ \phi_i}{\sum_i E_{\perp,i}} \tag{1}$$

where the sums run over all particles assigned to the jet.

2.1 Cone Algorithm

Based on the proposal of Sterman and Weinberg [8] many different implementations of cone algorithms have been developed. While the basic idea of the cone algorithm is simple and very intuitive, an operational definition is non-trivial. The resulting jet cross sections are depending on how the algorithm treats the choice of jet initiators and configurations of overlapping jet cones. It has repeatedly been pointed out that many definitions of cone algorithms are not infrared and/or collinear safe [9, 10].

In this analysis we use the definition implemented in the FORTRAN code PXCONE [11] which is considered experimentally and theoretically safe. This definition which corresponds closely to the Snowmass proposal [12] and to the algorithm used in the CDF experiment [13] is also used by the OPAL collaboration [14].

Jets are defined by the particles i within a cone of radius $R_0 = 1$ in pseudo-rapidity and azimuth space ($R_0^2 = \Delta\eta^2 + \Delta\phi^2$) around the jet axis. The algorithm operates as follows:

1. Each particle (or energy deposit in the detector) is considered as a seed of a jet.
2. The jet momentum is calculated from all particles within a radius R_0 around the seed direction using eq. (1).
3. If the jet direction differs from the seed direction, the jet direction is taken as the new seed direction and step 2 is repeated.
4. When the jet axis and the cone axis coincide and a stable jet direction is achieved the jet is stored in the list of "protojets" (if it is not identical with a protojet already found).
5. The steps 2 to 4 are repeated for all midpoints of pairs of protojets as seed directions[3]. This leads to infrared safety of the procedure [10].
6. Protojets with transverse energies of $E_{\perp,jet} < \epsilon$ are removed from the list.
7. All remaining protojets that have more than a fraction $ovlim$ of their transverse energy contained in a protojet of higher transverse energy are deleted.

[3]Practically it is sufficient to do this only for pairs of protojets with a distance between R_0 and $2\ R_0$.

8. All particles that are contained in more than one protojet are assigned to the protojet whose center is nearest in (η, ϕ). The jet momenta are recalculated using eq. (1).

9. All protojets with $E_{\perp,jet} < \epsilon$ are deleted and the remaining ones are called jets.

The jets with the highest transverse energies are considered in the analysis. Due to the last two steps it may happen that single particles within a jet have a distance larger than R_0 to the jet axis. This analysis is made with the parameter settings $\epsilon = 5\,\text{GeV}$ and $ovlim = 0.75$.

2.2 Longitudinally Invariant $k_\perp$ Algorithm

The ambiguities that occur for cone jet definitions (choice of seeds, overlapping cones) are principally avoided for cluster algorithms which successively recombine particles to jets. One definition of such an algorithm (proposed in [15] and implemented in the FORTRAN package KTCLUS [16]) has properties very similar to cone algorithms. As for the cone algorithm the clustering procedure is based on the longitudinally boost-invariant quantities $E_\perp, \Delta\eta, \Delta\phi$. Iteratively the minimum of all distances between particles is determined and either the corresponding pairs of particles are merged into pseudo-particles or single (pseudo-) particles are declared as jets. This process is iterated until no particles are left:

1. We start with a list of all particles (or energy deposits in the detector) and an empty list of jets.

2. For each particle i as well as for each pair of particles (i, j) the distances d_i and d_{ij} are calculated (we set $R_0 = 1$)

$$d_i = E_{\perp,i}^2\ R_0^2 \quad \text{and} \quad d_{ij} = \min(E_{\perp,i}^2, E_{\perp,j}^2)\ R_{i,j}^2 \quad \text{with} \quad R_{i,j}^2 = \Delta\eta_{ij}^2 + \Delta\varphi_{ij}^2\,. \quad (2)$$

3. The smallest value of all the d_i and d_{ij} is labeled d_{min}.

4. If d_{min} is a d_{ij}, the particles i and j are merged into a new particle using the recombination prescription in eq. (1) and removed from the list of particles.

5. If d_{min} is a d_i, the particle i is removed from the list of particles and added to the list of jets.

6. When no particles are left (i.e. all particles are included in jets) the procedure is finished. The last jets that entered the list are the ones with highest transverse energies which are considered in the analysis.

This definition implies that particles with $R_{i,j} < R_0$ are subsequently merged, so that all final jets are separated by distances $R_{i,j} > R_0$. It is still possible that particles inside a jet have a distance $R_{i,j} > R_0$ to the jet axis and that particles with $R_{i,j} < R_0$ are not part of the jet.

3 The Observables

3.1 The jet shape

The jet shape is defined as the average fractional transverse energy of the jet inside a subcone of radius r concentric around the jet axis

$$\Psi(r) \equiv \frac{1}{N_{jets}} \sum_{jets} \rho(r) \qquad \text{with:} \qquad \rho(r) \equiv \frac{\sum_{i \in jet, d_i < r} E_{\perp,i}}{E_{\perp,jet}}, \tag{3}$$

where $E_{\perp,i}$ is the transverse energy of a particle i with distance d_i to the jet axis and N_{jets} is the total number of jets in the sample. As proposed in [10], only particles assigned by the jet algorithm to the jet are considered.

Usually the denominator in the definition of ρ is given by the summed $E_\perp$ of all particles within a radius R_0 to the jet axis. This means that $\Psi(r/R_0 = 1) = 1$. In our definition of ρ the denominator is given by the transverse energy of the jet. Since neither for the cone nor for the $k_\perp$ definition all particles assigned to a jet are necessarily within a radius of $r/R_0 < 1$ to the jet axis, $\Psi(r/R_0 = 1)$ is not constrained to have the value of one. With this choice of our observable we are also sensitive to measure the amount of transverse jet energy outside the radius R_0 to the jet axis.

3.2 Subjet Multiplicities

A natural choice to study the internal jet structure with the $k_\perp$ cluster algorithm is the multiplicity of subjets, resolved at a resolution scale which is a fraction of the jet's transverse energy. For each jet in the sample the clustering procedure is repeated for all particles assigned to this jet. The clustering of particles is stopped when the distances D_{ij} between all particles i, j are above some cut-off y_{cut}

$$D_{ij} \;=\; \frac{\min(E_{\perp,i}^2, E_{\perp,j}^2)}{E_{\perp,jet}^2} \; \frac{\left(\Delta\eta_{ij}^2 + \Delta\varphi_{ij}^2\right)}{R_0^2} \;>\; y_{\text{cut}} \tag{4}$$

and the remaining (pseudo-)particles are called subjets. y_{cut} is a resolution parameter determining to which extend the internal jet structure is resolved. From this definition it follows that for $y_{\text{cut}} = 1$ no subjet is resolved (therefore the number of subjets is one), while for $y_{\text{cut}} \to 0$ every particle of the jet is resolved as a subjet. The observable that is studied in this analysis is the average number of subjets for a given value of the resolution parameter, $\langle N_{\text{subjet}} \rangle (y_{\text{cut}})$, where y_{cut} is in the range $10^{-3} \leq y_{\text{cut}} \leq 1$.

4 Monte Carlo Models

A simulation of the detailed properties of the hadronic final state is available in form of Monte Carlo event generators. They usually include the matrix element of the hard subprocess in first order of the strong coupling constant α_s, QCD radiation effects and a model to describe the non-perturbative transition from partons to hadrons.

The LEPTO Monte Carlo [17] incorporates the $\mathcal{O}(\alpha_s)$ QCD matrix element and takes higher order parton emissions approximately into account using the concept of parton showers [18] based on the leading logarithm DGLAP equations [19]. The QCD radiation can occur before and after the hard subprocess. The formation of hadrons is performed using the LUND string model [20] implemented in JETSET [21].

The HERWIG Monte Carlo [22] only differs in details from the above described QCD treatment and relies on leading logarithm parton showers with additional matrix element corrections [23]. It implements the cluster fragmentation model [24].

ARIADNE [25] treats the hard subprocess and the QCD shower evolution differently. Gluon emissions are treated by the colour dipole model [26] assuming a chain of independent radiating dipoles spanned by colour connected partons. The first emission in the cascade is corrected by the matrix element to first order α_s [27].

DJANGO [28] provides an interface between the event generator LEPTO or ARIADNE and HERACLES [29] which includes the full electroweak matrix element to calculate radiative corrections.

5 The H1 Detector

A detailed description of the H1 detector can be found elsewhere [30]. Here we briefly introduce the detector components relevant for this analysis: The liquid argon (LAr) calorimeter [31], the backward lead-scintillator calorimeter (BEMC) [32], and the tracking chamber system [33].

The hadronic energy flow is mainly measured by the LAr calorimeter extending over the polar angular range $4.4^\circ < \theta < 154^\circ$ with full azimuthal coverage. The polar angle θ is defined with respect to the proton beam direction ($+z$ axis). It consists of an electromagnetic section ($20 - 30$ radiation lengths) with lead absorbers and a hadronic section with steel absorbers. The total depth of both calorimeters varies between 4.5 and 8 interaction lengths. Test beam measurements of the LAr calorimeter modules show an energy resolution of $\sigma_E/E \approx 0.50/\sqrt{E\ [\mathrm{GeV}]} \oplus 0.02$ for charged pions [34]. The absolute scale of the hadronic energy is presently known to 4%, as determined e.g. from studies of the transverse momentum balance of the scattered positron and the hadronic final state in DIS events.

The scattered positron is detected by the BEMC calorimeter with a depth of 22.5 radiation lengths covering the backward region of the detector, $151^\circ < \theta < 176^\circ$. The electromagnetic energy scale is known to an accuracy of 1%.

The calorimeters are surrounded by a super-conducting solenoid providing a uniform magnetic field of 1.15 T parallel to the beam axis in the tracking region.

Charged particle tracks are measured in two concentric jet drift chamber modules (CJC), covering the polar angular range $15^\circ < \theta < 165^\circ$. A backward proportional chamber (BPC) with an angular acceptance of $155.5^\circ < \theta < 174.5^\circ$ serves to identify positrons. Using information from the BPC and the reconstructed event vertex the polar angle of the scattered positron is known to better than 5 mrad.

kinematical region for DIS events:	$E' > 11\,\mathrm{GeV}$ $156^\circ < \theta_{el} < 173^\circ$ $Q^2 > 10\,\mathrm{GeV}^2$ $y > 0.15$
selection cuts for the dijet sample:	$E_{\perp\mathrm{Breit}} > 5\,\mathrm{GeV}$ $-1 < \eta_{\mathrm{jet,lab}} < 2$
PXCONE: $\epsilon = 5\,\mathrm{GeV}$, $ovlim = 0.75$, $R_0 = 1$	KTCLUS: $R_0 = 1$

Table 1: Definition of the phase space investigated in this analysis.

6 Data Selection

The analysis is based on H1 data taken in 1994 corresponding to an integrated luminosity of $\mathcal{L}_{int} \simeq 2\,\mathrm{pb}^{-1}$. DIS events are selected where the scattered positron is measured in the acceptance region of the BEMC calorimeter at energies where trigger efficiencies are approximately $100\,\%$. To ensure a good identification of the scattered positron and suppress background from misidentified photoproduction events the following cuts are applied:

- The cluster of the positron candidate must have an energy-weighted mean transverse radius of $r_{\mathrm{clust}} < 5\,\mathrm{cm}$.
- A BPC signal within $5\,\mathrm{cm}$ of the straight line connecting the shower center with the event vertex is required.
- The reconstructed event vertex must be within $\pm 30\,\mathrm{cm}$ around the nominal position.
- The quantity $\sum(E - p_z)$ (the sum runs over all energy depositions in the calorimeter) is expected to be equal to twice the energy of the initial state positron. The cut $35\,\mathrm{GeV} < \sum(E - p_z) < 70\,\mathrm{GeV}$ reduces the contribution from photoproduction events as well as events where hard photons are radiated collinear to the incoming positron.

The event kinematics are calculated from the polar angle θ_{el} and the energy E' of the scattered positron via $Q^2_{el} = 2\,E_0\,E'_{el}\,(1 + \cos\theta_{el})$ and $y_{el} = 1 - \frac{E'_{el}}{2\,E_0}(1 - \cos\theta_{el})$. E_0 denotes the energy of the incoming positron. Events in the phase space defined in table 1 are selected.

Jets are defined by the algorithms described in section 2. The input for the jet algorithms consists of a combination of energy clusters from the calorimeter and track momenta measured in the central tracker (we will refer to these as “combined objects”). While the energy clusters are fully considered, the four momenta of each single track is only allowed to contribute up to a momentum of $350\,\mathrm{MeV}$. This procedure partly compensates for expected energy losses in the calorimeter measurement (dead material, noise thresholds etc.). It reduces the dependence of the jet finding efficiency on the pseudo-rapidity of the jet and improves the resolution of the transverse jet energy [35].

The combined objects are boosted to the Breit frame (defined by $\vec{q} + 2x_{Bj}\vec{P} = 0$, where $\vec{q}$ and $\vec{P}$ are the momenta of the exchanged boson and the incoming proton) where the jet algorithms are applied. We select events with (at least) two identified jets with transverse energies of $E_{\perp\mathrm{Breit}} > 5\,\mathrm{GeV}$ in $-1 < \eta_{\mathrm{jet,lab}} < 2$. The event sample for the longitudinally invariant $k_\perp$ algorithm (the cone algorithm) consists of 2045 (2657) dijet events.

7 Correction of the Data

The data are corrected for detector effects and electroweak radiation from the initial and the final state lepton (corresponding to the level of stable hadrons) in the kinematic region given in table 1. The detector response is determined using events from Monte Carlo event generators that were subjected to a detailed simulation of the H1 detector. The following event generators are used: ARIADNE4.8 [25] interfaced by DJANGO6.2 [28] (with and without the inclusion of electroweak corrections) and LEPTO6.4 [17]. Both generators give a good description of the kinematical variables of the inclusive DIS data sample as well as of the angular and transverse energy distributions of the jets. We also observe a very good description of the observables introduced in section 3.

The measured data points are corrected bin-by-bin for detector effects. The correction factors are independent of the inclusion of electroweak radiation effects as included in DJANGO. Their dependence on details of the modeling of the hadronic final state is taken into account by considering the difference between ARIADNE and LEPTO as uncertainty.

For the $k_\perp$ (cone) algorithm the corrections for $\Psi(r)$ are below $10\,\%$ ($13\,\%$) for subcone radii $r > 0.3$ and always below $27\,\%$ ($23\,\%$). The corrections for $\langle N_{\text{subjet}}\rangle(y_{\text{cut}})$ are always below 7%. The correction factors from both QCD models are in good agreement (they differ typically by not more than $2\,\%$) for the jet shapes as well as for the subjet multiplicities [36]. The final correction factors are taken as the mean values of both models, considering the spread as error. In addition we have varied the calibration of the hadronic energy scale in the data sample in the range of $\pm 4\%$ around the nominal value. The error is estimated as the maximal deviation from the results at the nominal value. For all observables it is at most 5%. The final error is calculated by adding the statistical errors, the error from the model dependence, and the error from the uncertainty of the hadronic energy scale in quadrature.

The background from misidentified photoproduction events is estimated with a sample of photoproduction events generated with PHOJET [37] and is found to be negligible.

8 Results

Both observables, the jet shape and the subjet multiplicity, do not show a visible dependence on the kinematic variables x_{Bj} and Q^2. We therefore study their variation on quantities directly related to single jets, i.e. the transverse jet momentum ($E_{\perp\text{Breit}}$) and the pseudo-rapidity region (η_{Breit}).

Studies based on the predictions of LEPTO have shown that both observables are largely influenced by hadronization [36]. A comparison to $\mathcal{O}(\alpha_s^2)$ calculations, where hadronization effects are not implemented, is therefore not meaningful.

8.1 Jet Shapes

The dependence of the jet shape on the transverse jet energy $E_{\perp\text{Breit}}$ and on the pseudo-rapidity η_{Breit} of the jet in the Breit frame is shown in Fig. 1 for the cone and for the $k_\perp$ algorithm. The jet shape $\Psi(r)$ rises more steeply near the jet axis, i.e. for low r, for higher $E_{\perp\text{Breit}}$. This means that jets become more collimated when $E_{\perp\text{Breit}}$ increases. Both studied jet algorithms show the same feature. The $E_{\perp\mathrm{Breit}}$ dependence is however more pronounced for the cone algorithm. The rise of $\Psi(r)$ with increasing $E_{\perp\mathrm{Breit}}$ is seen in all η_{Breit} regions. The $E_{\perp\mathrm{Breit}}$ dependence is stronger for jets towards the proton direction. As can be seen in Fig. 2, for constant $E_{\perp\mathrm{Breit}}$ jets are narrower (broader) towards the photon (proton) hemisphere. These dependences are smaller for increasing $E_{\perp\mathrm{Breit}}$. For the $k_\perp$ algorithm only little η_{Breit} dependence is seen for $E_{\perp\mathrm{Breit}} > 8$ GeV. A possible explanation for this behaviour is that the internal jet structure is influenced by particles close to or produced by QCD radiation near the proton remnant. At lower $E_{\perp\mathrm{Breit}}$ these particles at relatively low transverse momenta have a stronger influence.

Generally, jets defined by the $k_\perp$ algorithm are more collimated. The dependence on $E_{\perp\mathrm{Breit}}$ and η_{Breit} is stronger for the cone algorithm (see Fig. 3). In the forward region and for low $E_{\perp\mathrm{Breit}}$ jets the cone algorithm produces jets that are broader. Only in the region where the jets are relatively collimated ($E_{\perp\mathrm{Breit}} > 8$ GeV and $\eta_{\mathrm{Breit}} < 2.2$) both algorithms produce similar jet shapes.

As can be seen in Fig. 4, the jet shapes are well described by the QCD models. LEPTO shows the tendency to produce broader jets especially towards the proton remnant region ($\eta_{\mathrm{Breit}} > 2.2$). HERWIG produces jets which are too narrow, especially at large $E_{\perp\mathrm{Breit}}$ and η_{Breit}. ARIADNE lies between these two models in most cases and gives a good overall description of the data.

A concise summary of the observed dependence of the jet shape on $E_{\perp\mathrm{Breit}}$ and $\eta_{\mathrm{Breit}}$is shown in Fig. 7 where $\Psi(r)$ is shown at a fixed subcone radius of $r = 0.5$. Jets become more collimated with increasing $E_{\perp\mathrm{Breit}}$ and become broader towards the proton hemisphere. The η_{Breit} dependence is most pronounced for low $E_{\perp\mathrm{Breit}}$ jets.

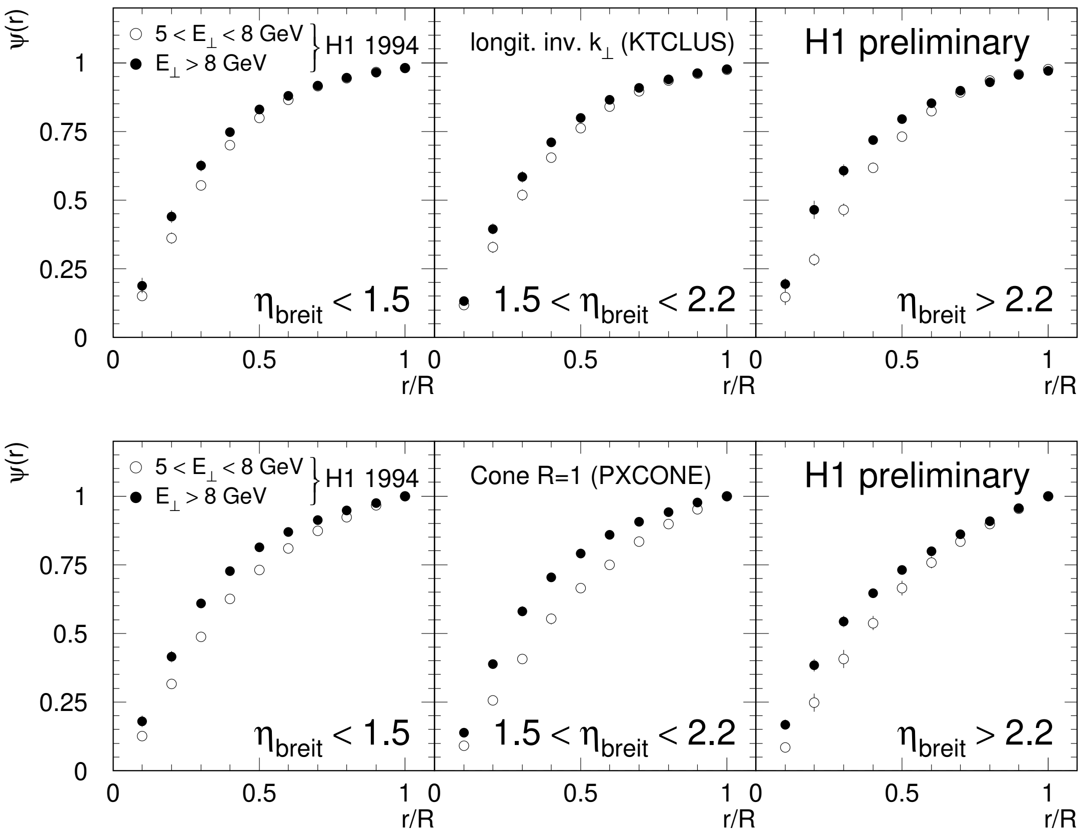

Figure 1: The dependence of the jet shapes on the transverse jet energy in three pseudo-rapidity regions. Overlaid are the jet shapes at higher and at lower transverse jet energies for the longitudinally invariant $k_\perp$ algorithm (top) and the cone algorithm (bottom). The comparison is shown as a function of the jet pseudo-rapidity in the Breit frame (positive pseudo-rapidities are towards the proton direction).

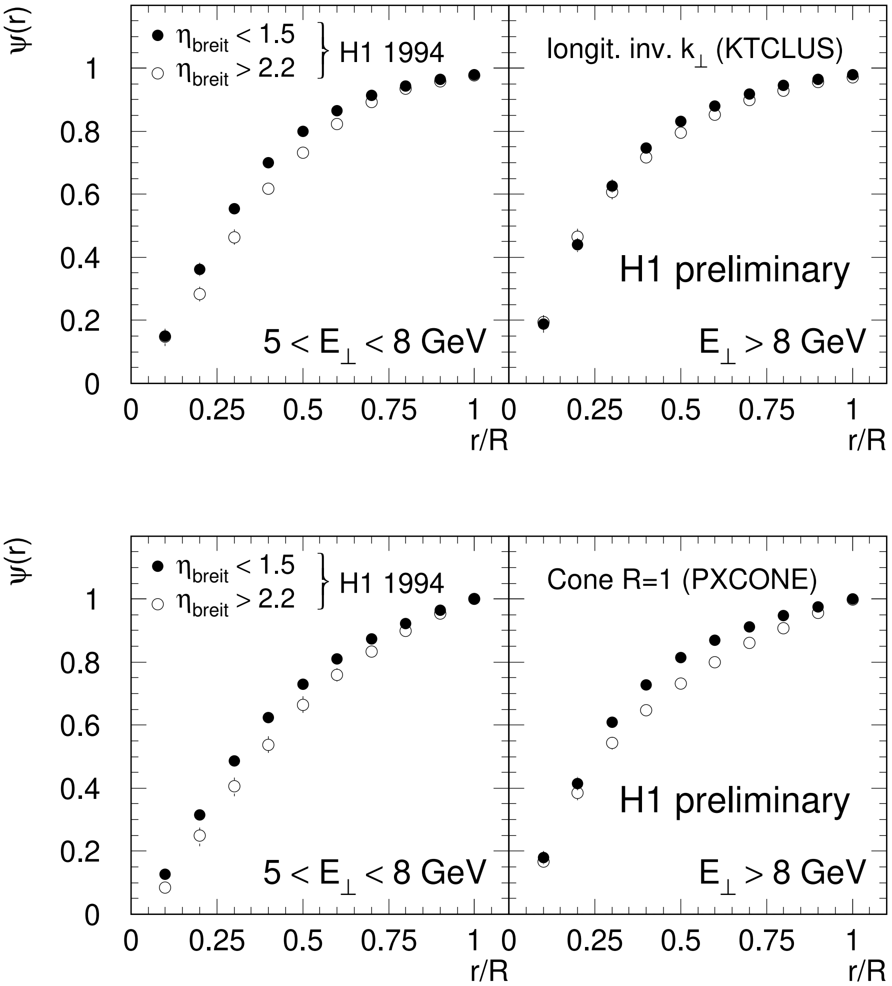

Figure 2: The dependence of the jet shapes on the pseudo-rapidity of the jet in the Breit frame (positive pseudo-rapidities are towards the proton direction). Overlaid are the jet shapes for forward and for backward jets for the longitudinally invariant $k_\perp$ algorithm (top) and the cone algorithm (bottom). The comparison is shown as a function of the transverse jet energy.

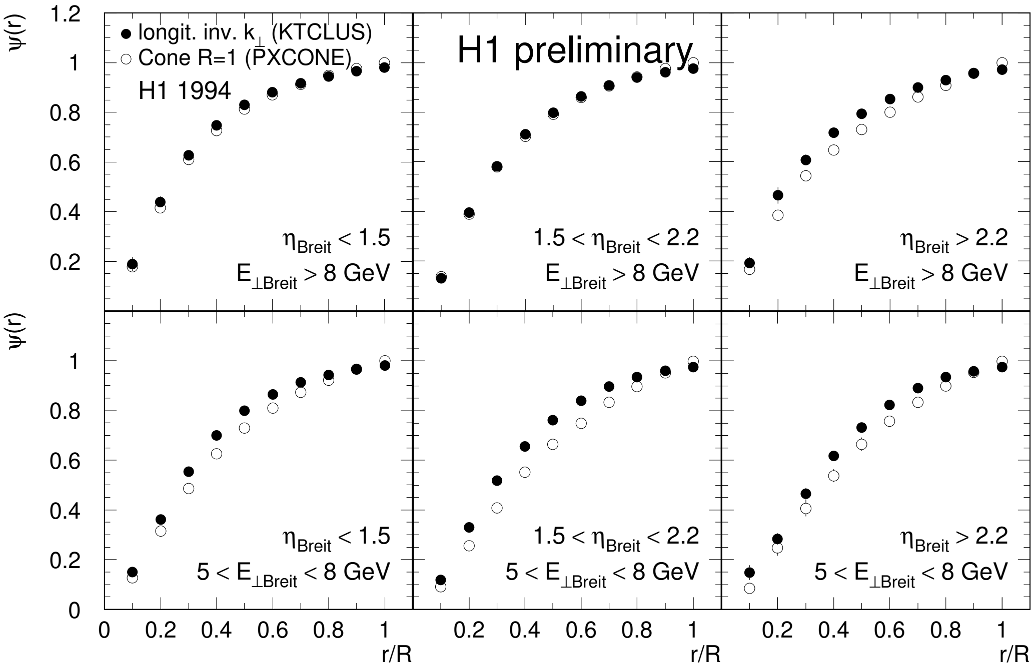

Figure 3: Comparison of the jet shapes for the longitudinally invariant $k_\perp$ algorithm and the cone algorithm. The data are shown as a function of the transverse jet energy and the jet pseudo-rapidity in the Breit frame (positive pseudo-rapidities are towards the proton direction).

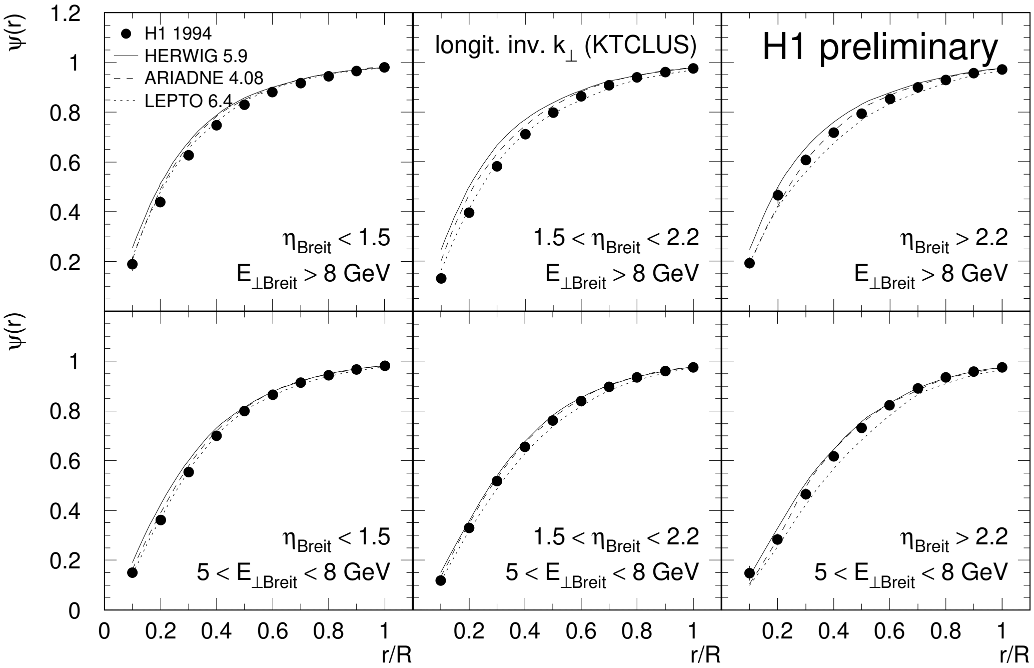

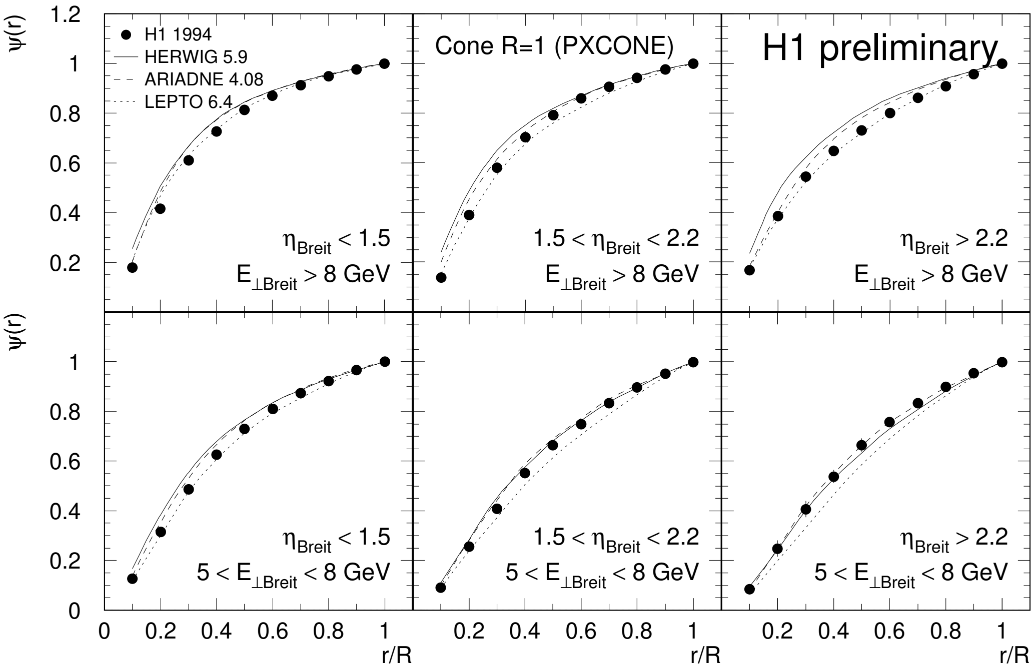

Figure 4: The jet shapes for the longitudinally invariant $k_\perp$ algorithm (top) and the cone algorithm (bottom). The data are shown as a function of the transverse jet energy and the jet pseudo-rapidity in the Breit frame (positive pseudo-rapidities are towards the proton direction). The results are compared to predictions of QCD models.

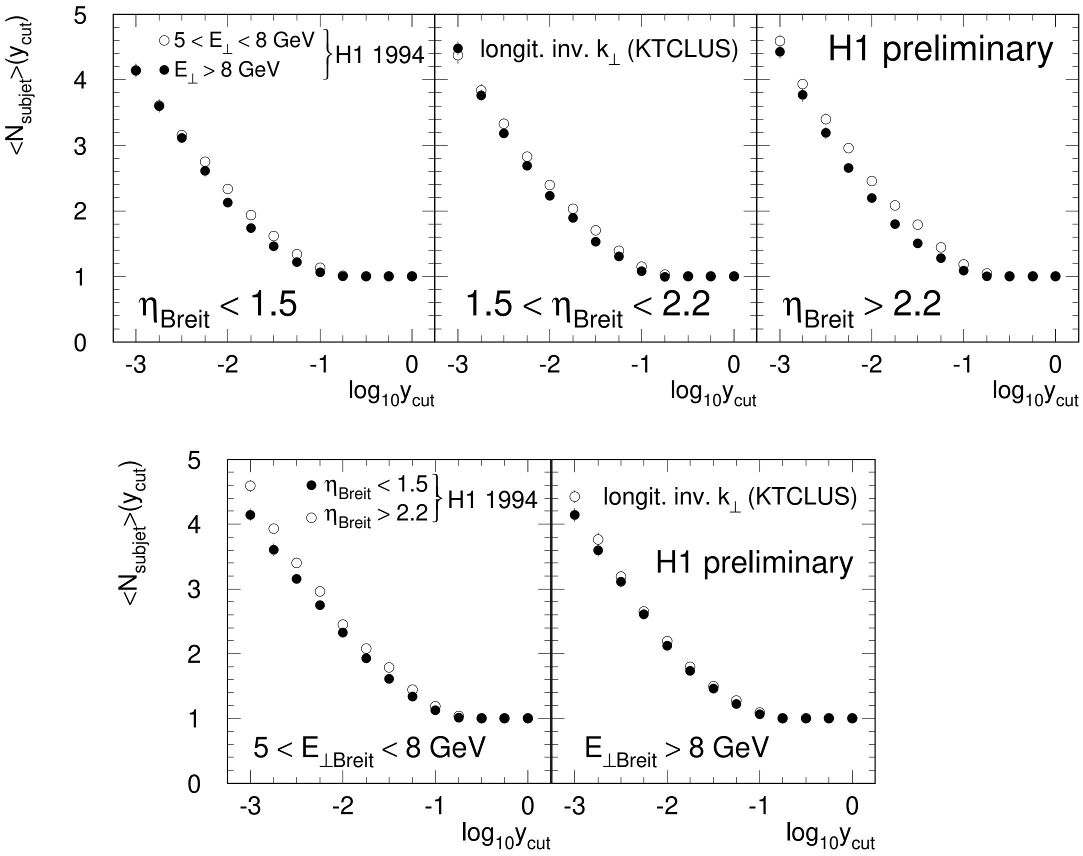

Figure 5: The average number of subjets as a function of the resolution parameter $y_{\rm cut}$ for the longitudinal invariant $k_\perp$ algorithm. The data are shown in $\eta_{\rm Breit}$ bins for different $E_{\perp\rm Breit}$ and in $E_{\perp\rm Breit}$ bins for different $\eta_{\rm Breit}$.

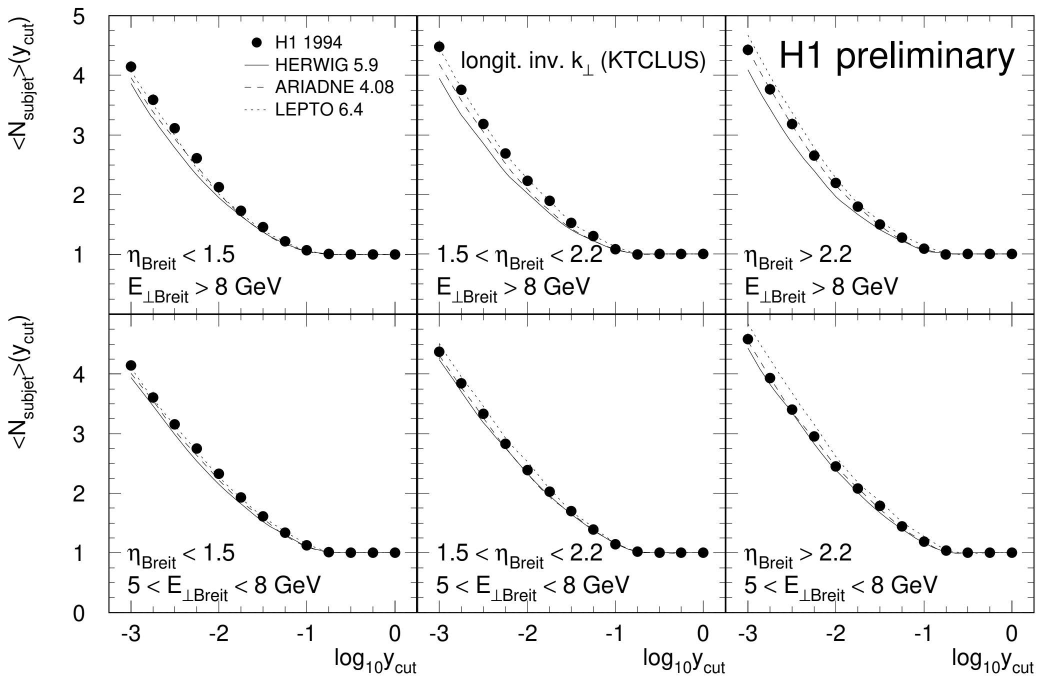

Figure 6: The average number of subjets as a function of the resolution parameter y_{cut} for the longitudinally invariant $k_\perp$ algorithm. The data are shown as a function of the transverse jet energy and the jet pseudo-rapidity in the Breit frame (positive pseudo-rapidities are towards the proton direction). The results are compared to predictions of QCD models.

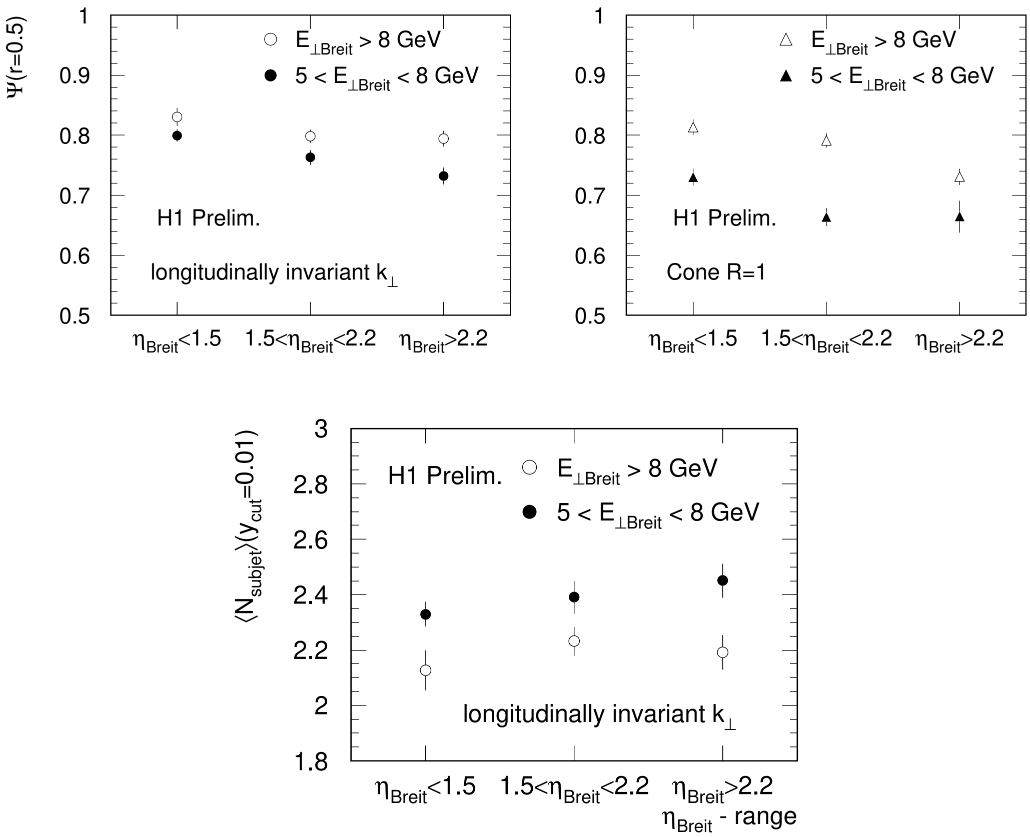

Figure 7: Upper figure: The jet shape $\Psi(r)$ at a fixed subcone radius $r = 0.5$ in three $\eta_{\rm Breit}$ ranges and two $E_{\perp \rm Breit}$ bins for the longitudinally boost invariant $k_\perp$ algorithm (left) and the cone algorithm (right). Lower figure: The mean subjet multiplicity at a fixed resolution parameter $y_{\rm cut} = 0.01$ in three $\eta_{\rm Breit}$ ranges and two $E_{\perp \rm Breit}$ bins for the longitudinally boost invariant $k_\perp$ algorithm. Positive pseudo-rapidities are towards the proton direction.

8.2 Subjet Multiplicities

In Fig. 5 the results of the subjet multiplicities are summarized. The main conclusions from the jet shape analysis can consistently be drawn for this observable. Higher subjet multiplicities are found at lower $E_{\perp \text{Breit}}$. This is most pronounced in the forward region ($\eta_{\text{Breit}} > 2.2$). For $\eta_{\text{Breit}} < 1.5$ this is only true for intermediate y_{cut} values of $10^{-2} \lesssim y_{\text{cut}} \lesssim 10^{-1}$. The subjet multiplicty increases towards the proton remnant. The strongest dependence is found at small y_{cut} and for low $E_{\perp \text{Breit}}$.

QCD models follow the gross feature of the data. Differences between the various models are largest at low y_{cut}. HERWIG predicts a subjet multiplicity which is too low at low y_{cut}. In particular, towards the proton direction and high $E_{\perp \text{Breit}}$ too few subjets are produced. LEPTO nicely follows the data for $\eta_{\text{Breit}} < 2.2$. For $\eta_{\text{Breit}} > 2.2$, however, the subjet multiplicity exceeds the data. This is independent of $E_{\perp \text{Breit}}$. ARIADNE gives a nice description of the data over the full considered phase space.

The mean subjet multiplicity for a given resolution parameter of $y_{\text{cut}} = 0.01$ is shown in Fig. 7. A higher $\langle N_{\text{subjet}} \rangle (y_{\text{cut}})$ is found for large $\eta_{\text{Breit}}$and lower $E_{\perp \text{Breit}}$.

9 Summary

Measurements of the internal jet structure in a dijet sample produced in deep-inelastic scattering have been presented in the kinematic domain $10 < Q^2 \lesssim 120\,\text{GeV}^2$ and $2 \cdot 10^{-4} \lesssim x_{Bj} \lesssim 8 \cdot 10^{-3}$. Jets found in the Breit frame using the cone and the $k_\perp$ algorithm were required to have $E_{\perp \text{Breit}} > 5$ GeV and $-1 < \eta_{\text{jet,lab}} < 2$.

Both observables, the jet shapes and subjet multiplicities, show that jets become more collimated with increasing $E_{\perp \text{Breit}}$. They become wider towards the proton remnant direction. The effect of this broadening is most pronounced at lower $E_{\perp \text{Breit}}$ and in the forward region. Jets defined by the cone algorithm are generally broader than the ones defined by the $k_\perp$ algorithm.

The internal jet structure is well described by the QCD models ARIADNE, HERWIG and LEPTO.

10 Acknowledgments

We are grateful to the HERA machine group whose outstanding efforts have made and continue to make this experiment possible. We thank the engineers and technicians for their work in constructing and now maintaining the H1 detector, our funding agencies for financial support, the DESY technical stuff for continual assistance, and the DESY directorate for the hospitality which they extend to the non-DESY members of the collaboration.

References

[1] V. Khoze and W. Ochs, Int. J. Mod. Phys. A 12 (1997) 2949; S. Lupia, W. Ochs, Phys. Lett. B418 (1998) 214.

[2] B. Webber,, Phys. Lett. 339 (1994) 148; Y. L. Dokshitzer and B. Webber, Phys. Lett. B352 (1995) 451; M. Dasgupta and B.R. Webber, Eur. Phys. J. C 1 (1998) 539.

[3] OPAL Collab., R. Akers et al., Z. Phys. C 63 (1994) 197; Z. Phys. C 68 (1995) 179; Z. Phys. C 69 (1996) 543; DELPHI Collab., P. Abreu et al., CERN-EP/98-24.

[4] D0 collab., S. Abachi et al., Phys. Lett. B 357 (1995) 500; CDF collab., F. Abe et al., Phys. Rev. Lett. 70 (1993) 713.

[5] H1 Collab., S. Aid et al.,, Z. Phys. C70 (1996) 17.

[6] ZEUS Collab., J.Breitweg et al. , Europ. Phys. J. C2 (1998) 61.

[7] ZEUS Collab., J. Breitweg et al., DESY 98-038, Hamburg 1998, subm. to Eur. Phys. J.

[8] G. Sterman and S. Weinberg, Phys. Rev. Lett. 39 (1977) 1436.

[9] D.E. Soper, in: Recontres des Moriond, Les Arc, France (1997) and hep-ph/9706320.

[10] M.H. Seymour, in: Les Rencontres de la Valée d' Aoste, La Thuile, France (1997) and Nucl. Phys. B 513 (1998) 269.

[11] L.A. del Pozo, PhD Thesis University of Cambridge, RALT-002, 1993.

[12] J. Huth et al., Proceedings of the Summer Study on High Energy Physics, Snowmass, Colorado, 1990, 134.

[13] CDF Collaboration, F. Abe et al., Phys. Rev. D 45 (1992) 1448.

[14] OPAL Collaboration, R. Akers et al., Z. Phys. C 63 (1994) 197 and Z. Phys. C 68 (1995) 179.

[15] S.D. Ellis and D.E. Soper,, Phys. Rev. D 48 (1993) 3160.

[16] S. Catani, Yu.L. Dokshitzer, M.H. Seymour and B.R. Webber, Nucl. Phys. B406 (1993) 187.

[17] G. Ingelman, A. Edin and J. Rathsman, Comp. Phys. Comm. 101 (1997) 108.

[18] M. Bengtsson and T. Sjöstrand, Z. Phys. C 37 (1998) 465; Sjöstrand, Proc. of the HERA workshop 1987, Hamburg Vol. 1 (1988) 149.

[19] V.N. Gribov and L.N. Lipatov, Sov. J. Nucl. Phys. 15 (1972) 438 and 675; Yu. L. Dokshitzer, Sov. Phys. JETP 46 (1977) 641; G. Altarelli and G. Parisi, Nucl. Phys. 126 (1977) 297.

[20] B. Andersson et al., Phys. Rep. 97 (1983) 31.

[21] T. Sjöstrand, Comp. Phys. Comm. 39 (1986) 347; T. Sjöstrand and M. Bengtsson, ibid. 43 (1987) 367.

[22] G. Marchinesi et al., Comp. Phys. Comm. 67 (1992) 465.

[23] M. Seymour, Nucl. Phys. B 436 (1995) 443.

[24] B.R. Webber, Nucl. Phys. B 238 (1984) 492.

[25] L. Lönnblad, Comp. Phys. Comm. 71 (1992) 15.

[26] G. Gustafson and Ulf Petterson, Nucl. Phys. B 306 (1988); G. Gustafson, Phys. Lett. B 175 (1986) 453; B. Andersson, G. Gustafson, L. Lönnblad and Ulf Petterson, Z. Phys. C 43 (1989) 625.

[27] L. Lönnblad, Z. Phys. C 65 (1995) 285.

[28] K. Charchula, G. Schuler, H. Spiesberger, Comp. Phys. Comm. 81 (1994) 381.

[29] A. Kwiatkowski, H. Spiesberger and H.-J. Möhring, Comp. Phys. Comm. 69 (1992) 155.

[30] H1 Collaboration, I. Abt et al., Nucl. Instr. and Meth. A 386 (1997) 310 and 348.

[31] H1 Calorimeter Group, B. Andrieu et al., Nucl. Instr. and Meth. A 336 (1993) 460.

[32] H1 BEMC group, J. Bán et al., Nucl. Instr. and Meth. A 372 (1996) 399.

[33] J. Bürger et al., Nucl. Inst. Meth. A 279 (1989) 217; H1 FTD group, S. Burke et al., Nucl. Inst. Meth. A 313 (1996) 373.

[34] H1 Calorimeter Group, B. Andrieu et al., Nucl. Instr. and Meth. A 372 (1996) 399.

[35] J. Spiekermann, Ph. D. Thesis, University of Dortmund, unpublished; H. Rick, Ph. D. Thesis, University of Dortmund, unpublished.

[36] L. Sonnenschein, Diploma-thesis, PITHA 98/4, Aachen (Germany) March 1998.

[37] R. Engel, Z. Phys. C 66 (1995) 203; R. Engel and J. Ranft, Phys. Rev. D 54 (1996) 4244.